INORGANIC CHEMISTRY
FRONTIERS

CHINESE CHEMICAL SOCIETY
ROYAL SOCIETY OF CHEMISTRY

RESEARCH ARTICLE

View Article Online
View Journal | View Issue

Check for updates

Cite this: *Inorg. Chem. Front.*, 2025, **12**, 8676

Thermally responsive magnetic bistability through solid–liquid phase transitions in alkylthio-functionalized dithiadiazolyl radicals

Juho M. Toivola,[a] Ankita Naik,[a] Manu Lahtinen,[b] Oriol Gonzàlez-Prats,[a] Andrea Perez Prieto,[a] Itziar Oyarzabal *[c,d] and Aaron Mailman *[a]

Received 28th June 2025,
Accepted 27th September 2025

DOI: 10.1039/d5qi01391g

rsc.li/frontiers-inorganic

A series of *p*-alkylthio-substituted phenyl-1,2,3,5-dithiadiazolyl radicals, *p*-R-PhDTDA (R = SMe (**2**), SEt (**3**), S^{n}Pr (**4**), S^{i}Pr (**5**), S^{t}Bu (**6**)), and the prototypical (R = H (**1**)) phenyl derivative exhibit a thermally driven solid–liquid transition accompanied by a spin-state change from diamagnetic ($S = 0$) π-dimers to a pair of paramagnetic ($S = \frac{1}{2}$) radicals. X-ray crystallography reveals that most derivatives form phase-pure *cis*-cofacial dimers, except **3** which crystallizes as three distinct polymorphs: $\mathbf{3\alpha}$ displays a sandwich-type herringbone structure stabilized by intermolecular S⋯S chalcogen bonding (isostructural with **2**) while $\mathbf{3\beta}$ and $\mathbf{3\gamma}$ feature slipped π-stacked herringbone arrangements (ABAB and AA′BB′, respectively). In these latter forms, the alkyl groups act as steric buffers between adjacent stacks, a structural motif retained in derivatives **4–6**. Differential scanning calorimetry (DSC), hot-stage microscopy, and vibrating sample magnetometry (VSM) collectively demonstrate a hysteretic phase transition in **1–6** with magnetic bistability arising from supercooling of the paramagnetic liquid phase. These results establish a new design paradigm for stimuli-responsive materials in which molecular packing, thermal behavior, and spin states are intrinsically linked through phase transitions.

Introduction

Thiazyl radicals have emerged as highly attractive building blocks for advanced molecular materials, owing to their intriguing magnetic properties, tunable electronic structures, and diverse solid-state packing arrangements.[1–8] Well-studied examples include 1,2,3,5- and 1,3,2,5-dithiadiazolyl (DTDA) radicals (**A–D**, **L–O**) and 1,3,2-dithiazolyls (1,3,2-DTA, **E**, **F**, **K**), which exhibit distinct electronic and structural behaviors (Scheme 1).[9–18] The asymmetric 1,3,2,5-DTDAs (**A**) are less common due to photochemically allowed rearrangement to the thermodynamically favored 1,2,3,5-DTDA derivatives (**B–D**, **L–O**). A key advantage of these thiazyl radicals lies in their structural diversity, which allows for fine-tuning of their electronic properties.[19,20] Both 1,3,2-DTAs and 1,3,2,5-DTDAs exhibit substituent-dependent electronic structures, allowing for deliberate modulation of their magnetic and conductive properties.[21–24] In contrast, the widely accessible 1,2,3,5-DTDA displays electronic structures that remain largely substituent-

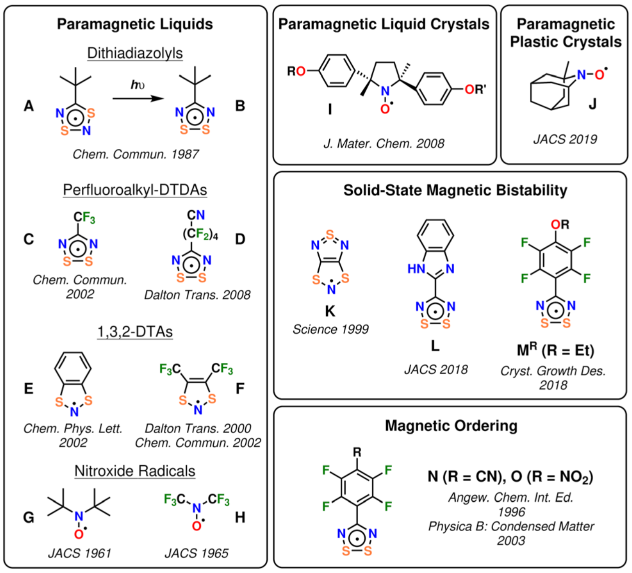

Scheme 1 Selected examples of different classes of radicals exhibiting melt-recrystallization behavior, magnetic bistability, or magnetic ordering.

---

[a] University of Jyväskylä, Department of Chemistry, NanoScience Centre, P.O. Box 35, FI-40014 Jyväskylä, Finland. E-mail: aaronmailman@gmail.com, aaron.m.mailman@jyu.fi
[b] University of Jyväskylä, Department of Chemistry, P.O. Box 35, FI-40014 Jyväskylä, Finland
[c] BCMaterials, Basque Center for Materials, Applications and Nanostructures, UPV/EHU Science Park, ES-48940 Leioa, Spain.
E-mail: itziar.oyarzabal@bcmaterials.net
[d] Ikerbasque, Basque Foundation for Science, ES-48009 Bilbao, Spain

independent due to the nodal nature of their single occupied molecular orbital (SOMO). As a result, their bulk properties are primarily governed by molecular packing rather than intrinsic electronic modifications.[25–27] This dichotomy underscores the critical role of crystal engineering in optimizing the functional behavior of thiazyl-based materials, which is a persistent challenge in their chemical development despite extensive research.[3,28]

A major feature of thiazyl radicals is their tendency to display magnetic bistability, where hysteretic spin-state transitions occur under thermal, pressure, or light stimuli.[14,15,29–34] Nitroxide radicals (**G–J**) are well-studied because of their stability and tendency to associate *via* weak intermolecular interactions rather than strong electronic reorganization, such as dimerization *via* covalent bond formation.[35–38] Their stability and synthetic versatility have made them model systems for studying spin-labeled soft materials, including liquid crystals and polymers.[37,39–41] Early studies of nitroxides revealed that melting-induced spin disordering could be harnessed in paramagnetic liquid crystals, offering tunable magnetic responses in fluid phase (**I**).[37] Recent work on sterically hindered adamantly functionalized nitroxides demonstrated a plastic crystalline state which undergoes a single-crystal-to-single-crystal (SCSC) transition with retention of crystallinity (**J**).[38] Here, dynamic disorder in the high-temperature phase allows for reversible spin switching, a phenomenon with parallels in spin-crossover complexes.[42]

To date, 1,3,2-DTA radicals have frequently exhibited SCSC transitions, reversibly switching between diamagnetic (S = 0) dimers stabilized by multi-centered S⋯S interactions ('pancake-bonding') and pairs of paramagnetic ($S = \frac{1}{2}$) monomers enabled by thermal cleavage and reformation of chalcogen bonds.[30] The prototypical example is TTTA (1,3,5-trithia-2,4,6-triazapentalenyl, **K**) which undergoes a hysteretic spin transition near room temperature (Scheme 1). This transition is governed by a competition between spin-Peierls-like dimerization (stabilizing the diamagnetic state) and vibrational entropy (favoring the paramagnetic state at high temperatures) leading to a cooperative switching behavior with a pronounced thermal hysteresis loop.[14,31,32] These systems are highly tunable *via* substituent effects, enabling control over transition temperatures and hysteresis widths, however, their broader application is hindered by air sensitivity (compared to nitroxides) and synthetic scalability challenges.

In contrast, the related 1,2,3,5-DTDAs are readily synthesized and frequently display hysteretic melt-recrystallization phase transitions where the dimerized solids (S = 0) reversibly convert into paramagnetic ($S = \frac{1}{2}$) liquids.[10,11,43,44] Classic examples include **C** and **D**, where thermal dissociation of the dimers generates a paramagnetic liquid phase which subsequently recrystallizes upon cooling into a diamagnetic (S = 0) dimerized solid.[10,11] This reversible phase transition highlights the critical role of dynamic chalcogen bonding in modulating spin states and material properties. Despite their high propensity for polymorphism, SCSC transitions in DTDAs remain rare (*e.g.* **L** and $\mathbf{M^R}$; R = Et), likely due to their greater structural flexibility and weaker directional interactions compared to DTAs.[5,15,16] Recent studies have uncovered first-order phase transitions in DTDAs involving solid–liquid–solid (SLS) transformations, where melting disrupts dimeric interactions, yielding a paramagnetic liquid phase.[6,12,16] Recrystallization occurs *via* nucleation and growth, often leading to new polymorphs with distinct magnetic properties. This behavior is mechanistically distinct from SCSC transitions, as it involves loss of long-range disorder followed by reorganization into the same or different crystalline phases. Kinetic control over recrystallization opens pathways to metastable polymorphs which could be exploited for multistate magnetic switching alongside switching of conductivity or optical properties suggesting multifunctional applications.[45]

The 1,2,3,5-dithiadiazolyl (DTDA) framework is notable for the nodal character of its SOMO, which localizes the unpaired electron to the sulfur and nitrogen atoms, preventing full delocalization. This electronic configuration facilitates diverse dimerization modes, including *cis*, *trans*, *trans-antarafacial*, twisted, and orthogonal arrangements. Among these, the *cis*-cofacial dimers dominate, representing over 50% of reported structures.[46] However, the weak dimerization (~−35 kJ mol^{-1}) and small energetic differences between motifs leads to a diverse structural landscape (polymorphism).[6,11] In the absence of steric hinderance or structure directing groups, multiple dimerization motifs can coexist or interconvert, playing a key role in the phase transitions and/or polymorphism observed in these systems.[47–49]

The DTDA heterocycle and its dimers exhibit a feature-rich electrostatic potential (ESP) landscape, making them ideal for crystal engineering strategies (Scheme 2).[3,50,51] A well-defined σ-hole is observed at the S–S bond centroid of the DTDA monomer, characterized by an electropositive region that engages in chalcogen bonding with electron-rich acceptors (*e.g.* cyano or nitro groups, as seen in compounds **N** and **O**). This interaction parallels classical halogen bonding but with enhanced directionality due to the polarizable sulfur centers.[52–55]

In the DTDA π-dimers the σ-hole becomes more pronounced and delocalized, facilitated by multi-centered S⋯S interactions (see Scheme 2, Fig. 1 and 2 for ESP maps). Unlike the localized σ-holes in halogen bonds, this delocalized elec-

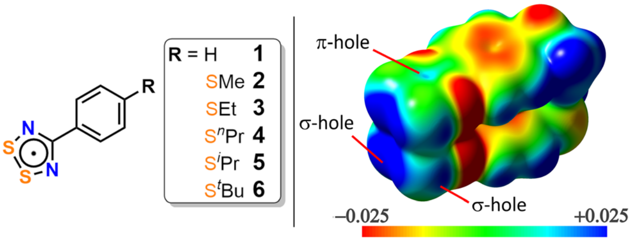

Scheme 2 (Left): The *p*-substituted phenyl-1,2,3,5-dithiadiazolyl radicals investigated in this study. (Right): Electrostatic potential (ESP) mapped onto the electron density isosurface (0.002 a.u.) around a *cis*-cofacial dimer of **2** highlighting the feature-rich electropositive (blue) and electronegative (red) regions.

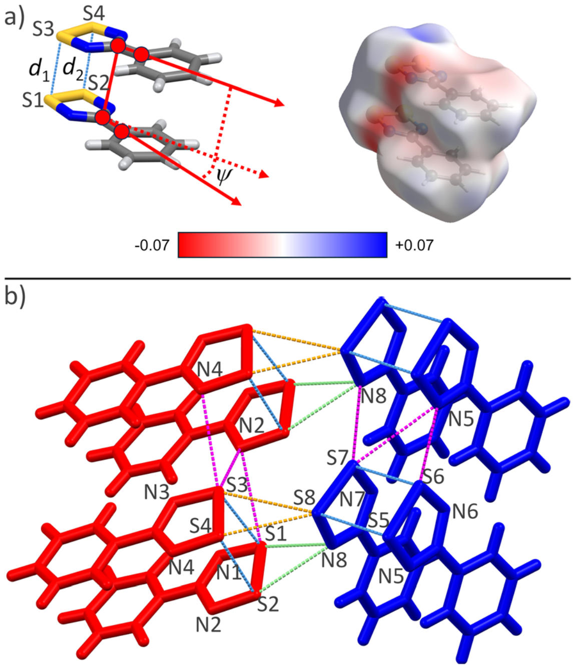

Fig. 1 Molecular structure and intermolecular interactions in compound **1**. (a) Side view of a crystallograpically independent dimer, showing the torsion angle ψ and the electrostatic potential (ESP, range: −0.07 to 0.07 a.u.) mapped onto its Hirshfeld surface. (b) View of the two crystallographically independent dimers (colored red and blue), highlighting the network of key intermolecular contacts: intradimer S⋯S′ (light blue, d_1/d_2), interdimer S⋯S′ (orange, d_3/d_4); full metric details given in Table 1. Selected **SN-I** and **SN-III** contacts (green and magenta): S1⋯N8 = 3.155(3), S2⋯N8 = 3.103(3), S1⋯N2 = 3.534(2), S3⋯N2 = 3.324(2), S3⋯N4 = 3.509(2), S6⋯N5 = 3.506(3), S7⋯N5 = 3.517(3), S7⋯N8 = 3.524(3) Å.

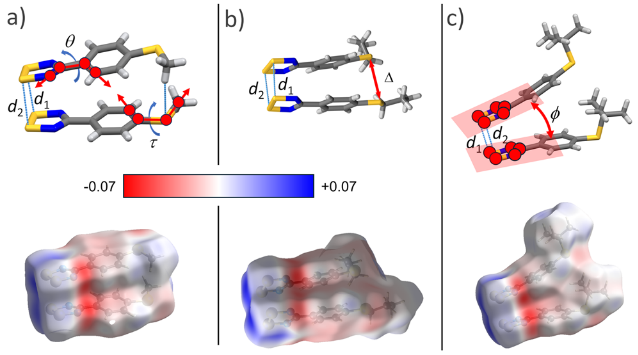

Fig. 2 Structural diversity of *cis*-cofacial π-dimers and their intermolecular interaction landscapes. (a) The dimer in **2** illustrates key geometric parameters: the twist angle (θ) between π-planes and the C–C–S–C dihedral angle (τ). (b) In **4**, the intradimer S⋯S′ distance (Δ) is a metric for describing dimer geometry (disorder omitted for clarity). (c) The dimer in **6** demonstrates steric accommodation of bulky ^{t}Bu-groups and illustrates the hinge angle ϕ. For each dimer, the associated electrostatic potential (ESP) mapped onto the Hirshfeld surface reveals the nature and polarity of key intermolecular contacts.

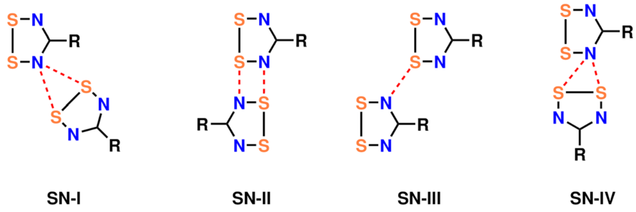

Chart 1 Common in-plane electrostatic interactions between DTDAs.

tropositive regions (blue in ESP plots) arises from cooperative σ-hole/π-hole overlap and orbital mixing within the dimer. Additionally, weaker σ-holes along the extension of the S–S bond axis enable additional S⋯N interactions (Chart 1), further diversifying the supramolecular assemblies.

Despite their central role in the crystal engineering of organic radicals, the influence of the substituents on the solid-state packing of DTDA derivatives remains relatively underexplored.[56,57] Prior studies have primarily focused on general structural motifs, often overlooking the nuanced impact of functional group variation on intermolecular interactions and crystal packing.[16,44] Similarly, investigations into chalcogen bonding in DTDAs have largely been confined to S⋯N contacts, as highlighted in Chart 1, and occasional interactions involving substituents, leaving ample room for a more comprehensive understanding of non-covalent interactions in these systems.[58]

In addition to their rich solid-state chemistry, DTDAs are among the few organic radicals to exhibit stable paramagnetic liquid phases.[10,11,43,44] However, the thermal behavior of these materials, particularly phenomena such as supercooling and phase-dependent magnetic bistability, has not been systematically studied across structurally related derivatives. In this work, we present a detailed investigation of solid–liquid phase transitions and their magnetic consequences in a homologous series of *para*-substituted phenyl-DTDAs (*p*-R-PhDTDA) where R = H (**1**), SMe (**2**), SEt (**3**), S^{n}Pr (**4**), S^{i}Pr (**5**), and S^{t}Bu (**6**) given in Scheme 2. This series provides a controlled platform to examine the role of steric and electron factors in modulating both intermolecular interactions and phase-dependent magnetic behavior.

Results and discussion

Synthetic procedures

The *p*-alkylthiobenzonitrile precursors, *p*-RS-Ph-CN were readily prepared by nucleophilic aromatic substitution of 4-fluorobenzonitrile with the corresponding sodium alkylthiolates (R = Et, ^{n}Pr, ^{i}Pr and ^{t}Bu) yielding moderate to high yields after purification by fractional vacuum distillation, except for R = Me, which was commercially obtained (SI). Following established synthetic methodologies, these nitriles were converted to the persilylated amidines[59] and purified by fractional vacuum distillation or recrystallization to afford spectroscopically pure compounds, as pale-yellow oils or waxy white solids. Cyclocondensation of the persilylated amidines with sulfur monochloride (S_2Cl_2) in MeCN produced the corresponding dithiazolylium chloride salts **2**[Cl]–**6**[Cl] as sparingly soluble orange solids. Reduction of these chloride salts with a small excess of triphenylantimony ($SbPh_3$) in degassed acetonitrile (MeCN) afforded the target radicals *p*-RS-PhDTDA (**2–6**) as crystalline solids at room temperature. The prototypical radical, phenyl-DTDA (**1**), was synthesized by a modification of a literature method (SI).

All radicals **1–6** were purified by three-zone temperature gradient sublimation under dynamic vacuum (10^{-3} mbar) to afford analytically pure, crystalline solids suitable for thermal and magnetic characterization (Table S1). Full crystallographic details are given in SI.

Crystal structures and packing motifs

Crystal structure of prototypical radical 1. The dark orange coloured needles (in reflected light), violet (in transmitted light) of **1** suitable for single-crystal X-ray diffraction (SCXRD) analysis crystallize in the chiral orthorhombic space group $P2_12_12_1$ (Table S2),[60] featuring two crystallographically independent *cis*-cofacial π-dimers in the asymmetric unit, as illustrated in Fig. 1a. The key intradimer S⋯S′ distances (d_1 = 3.033(1), 3.089(1) and d_2 = 3.108(1), 3.179(1) Å; Table 1), are significantly shorter than the sum of the sulfur van der Waals radii (∑vdW = 3.6 Å) indicating strong dimerization between the DTDA rings.[61–63]

Each dimer geometry is defined by hinge angles ($\phi \approx 7.1°$ and $\phi' \approx 6.9°$) between the mean planes of each DTDA ring and torsion angles ($\psi \approx 4.5(2)°$ and $\psi \approx 8.3(2)°$) through the C_4 linkage, which confirms a near collinear alignment of the radicals, as illustrated in Fig. 1a. The DTDA-phenyl ring twist angle between mean planes through each ring ($\theta \approx 8.3°$), reflects a shallow rotational barrier[64] contrasting sharply with *ortho*-fluorinated analogy ($\theta \approx 30°$) where steric repulsion between the nitrogen and fluorine lone pairs dominates.[64]

The solid-state architecture of the unsubstituted prototypical radical **1** is stabilized by a rich and extensive network of intermolecular interactions, as illustrated in Fig. 1b. The absence of sterically demanding substituents facilitates dense, efficient packing, which is dominated by directional σ-hole interactions and a combination of **SN-I** and **SN-III** type interactions (Chart 1), which work in concert to create a cohesive, three-dimensional framework. This intricate interplay of interactions highlights the innate propensity of the radical core to form stable, well-defined supramolecular architectures.

These metrics are compiled in Table 1 and highlight how subtle changes in the substitution of the phenyl ring may dramatically influence the conformation and packing in dithiadiazolyl (DTDA) systems.

Crystallization of 2 and polymorphs of 3. Large, lustrous green blocks of **2** suitable for SCXRD were obtained from the middle zone of a three-zone sublimation (303–323–353 K; see Tables S1 and S2). The methyl derivative **2** crystallizes in the acentric space group $P2_1$. For the ethyl derivative **3**, two distinct polymorphs were initially isolated as a mixture from the reduction of the crude chloride salt with $SbPh_3$ in MeCN: **3α** (lustrous green blocks in reflected, dark orange in transmitted) and **3β** (dark orange parallelogram-shaped plates) as confirmed by powder X-ray diffraction (PXRD; see Fig. S9). The alpha-phase, **3α** crystallizes in the monoclinic space group $P2_1/c$, while **3β** crystallizes in the *Pn* space group (Table S3).

Repeated three-zone, temperature gradient sublimation (303–343–363 K) affords **3α** (343 K middle zone) and a new phase, **3γ** (303 K, lowest temperature zone) as phase-pure compounds (PXRD, see Fig. S10 and S13). The small orange plates of **3γ** appear dark green in reflected light but are not as lustrous as **3α**. Despite their smaller size, high-quality, single-crystal X-ray diffraction data was obtained (see Table S3) for the gamma-phase, which crystallizes in the monoclinic space group $P2_1/n$ (Table S3).

Interestingly, recrystallization of analytically pure **3** from MeCN affords the **3γ** as the principal phase, whereas recrystallization from EtCN affords **3β**. The latter is also obtained as the dominant phase when sublimed onto a cold substrate (~285 K) under static vacuum (10^{-3} mbar). Moreover, DSC reveals that the melt-recrystallization of **3** predominantly yields the **3β** phase, as confirmed by both post-DSC single-crystal and powder X-ray diffraction measurements (see Fig. S11).

Table 1 Select structural parameters from **1–6** [a]

	θ	τ	ϕ	ψ	d_1	d_2	Δ	d_3	d_4
1	8.3	—	7.07	4.5(2)	3.033(1)	3.108(1)		3.406(1)	3.602(1)
		—	6.89	8.3(2)	3.089(1)	3.179(1)			
2	13.2	5.1	7.79	4.5(2)	3.1496(7)	3.0209(7)	4.4349(9)	**3.2912(8)**	**3.4129(8)**
3α	9.5	6.6	4.41	2.3(1)	3.0908(6)	3.1350(7)	4.7671(7)	**3.3544(7)**	**3.5211(7)**
3β	7.1	2.6	5.09	6.2(4)	3.040(2)	3.085(2)	4.305(2)	3.505(2)	3.413(2)
3γ	7.3	3.8	5.52	6.3(5)	3.075(2)	3.102(2)	4.459(3)	3.518(2)	3.415(2)
4	7.9	6.4	5.61	8.1(2)	3.079(1)	3.092(1)	4.510(4)	3.546(1)	3.413(1)
5	10.1	62.5	6.44	0.4(2)	3.079(1)	3.076(1)	5.168(1)	3.5479(9)	3.4466(9)
6	11.6	89.7	8.32	1.4(2)	3.063(1)	3.086(1)	6.103(1)	3.476(1)	3.613(1)

[a] Definition of metrical parameters; monomeric parameters: θ (theta): the twist angle between mean planes of the phenyl and DTDA rings; τ(tau): the dihedral angle between the plane of the phenyl ring and the $C–S–C^{Ph}$ plane of the thioalkyl group (C is the methyl/methylene carbon). Dimeric parameters: ϕ(phi): the hinge angle between mean planes of the two DTDA rings in a dimeric unit; ψ(psi): the torsion angle along the $C^{DTDA}–C_4$ bond axis of both radicals in the dimer, defining the collinearity; Δ(delta): the intradimer S⋯S′ distance (Å) between exocyclic sulfur atoms. d_1/d_2: intradimer S⋯S′ distances (Å) where d_1 corresponds to $d(S_1 \cdots S_3)$ and d_2 $d(S_2 \cdots S_4)$ in the *cis*-cofacial dimers. Interdimer packing: d_3/d_4: key interdimer S⋯S′ distances (Å), denoting interactions between a DTDA and either another DTDA or a thioalkyl sulfur atom (given in bold text) from a neighboring molecule. See illustrative examples in Fig. 1 and 2.

Single crystals of **4–6** were grown only by three-zone gradient vacuum sublimation (Table S1) and single crystal parameters are given in Table S4.

Common structural features. All compounds **1–6** crystallize as *cis*-cofacial π-dimers, a common motif for such radicals, characterized by intradimer S⋯S′ contacts ($d_1(S_1\cdots S_3)$, $d_2(S_2\cdots S_4)$; Table 1) significantly shorter than the sum of the van der Waals raii ($\sum$vdW = 3.6 Å). These close contacts are characteristic of such dimers and are consistent with those found in related dithiadiazolyl (DTDA) systems. A fundamental distinction from their alkoxy analogues (**M^R^**; R = Me–Bu, ω = 118–122°) is the notably less obtuse average C–S–C bond angle ($\omega \approx$ 104–105°) which reflects reduced s–p orbital hybridization at the sulfur atom in the thioether group.[65] Within the thioalkyl series, the specific conformation of the –SR group exerts a profound influence on the dimer geometry, primarily through the C–C–S–C dihedral angle (τ) and the torsion angle between radicals (ψ) which in turn dictate the S⋯S′ distance (Δ). A more detailed analysis of the molecular geometries and packing motifs of **2–6** is given in the is also given in the SI (section 7).

Low-steric impact, planar chains. Compounds with small, planar oriented alkyl groups achieve the most efficient packing. In **2** the methyl groups are nearly coplanar with the phenyl rings ($\tau \approx$ 5.1°) and adopt an antiparallel alignment, minimizing steric clash (Fig. 2a). This results in a small hinge angle ($\phi \approx$ 7.79°), near-collinear alignment of radicals ($\psi \approx$ 4.5(2)°) and an intermediate S⋯S′ distance (Δ = 4.4349(9) Å; Table 1). A similar, yet optimized, geometry is observed in **3β** where both ethyl groups are coplanar ($\tau \approx$ 2.6°) and oriented antiparallel, yielding the shortest S⋯⋯S′ distance (Δ = 4.305(2) Å) in the series (Table 1). The overall dimer metrics of **3β** and **3γ** are very similar but the packing motifs are distinct (*vide infra*). This demonstrates that well-organized ethyl chains in **3β** and **3γ** can facilitate closer contacts than a methyl group, which leads to the largest twist angle (θ = 13.2°) for **2**.

Disordered and *gauche*-oriented chains. The introduction of conformational flexibility or *gauche* orientations leads to subtle distortions. In **4**, the longer propyl chain is disordered and adopts a *gauche* conformation akin to one of the ethyl groups in **3α** (Fig. 2b). This increases the torsion angle to the largest in the thioalkyl series **2–6** (ψ = 8.1(2)°), resulting in a longer S⋯S′ distance (Δ = 4.510(4) Å) despite otherwise comparable parameters ($\tau \approx$ 6.4°, θ = 7.9°). The alpha-phase, **3α** itself presents a unique case where one EtS-group is coplanar ($\tau \approx$ 6.6°) while the other is *gauche*, forcing a near-perpendicular orientation. This asymmetry creates a pronounced bowing of one radical, leading to a surprisingly small hinge angle (ϕ = 4.41°) but a very long S⋯S′ separation (Δ = 4.7671(7) Å).

High-steric impact, branched chains. Branched alkyl groups introduce severe steric constraints that dominate the dimer structure. The isopropyl group in **5** forces a drastic deviation from coplanarity ($\tau \approx$ 62.5°). While the radicals remain remarkably collinear ($\psi \approx$ 0.4(2)°) and the rings coplanar (ϕ = 6.44°), the steric bulk is relieved through a large S⋯S′ distance (Δ = 5.168(2) Å), an increased twist angle (θ = 10.1°), and a pronounced bowing of one radical in the dimer. The *tert*-butyl group in **6** has an even more extreme steric impact. To avoid overwhelming steric clash, the system adopts a highly unusual conformation with an acute C–S–C angle ($\omega \approx$ 103.25°) and a near-orthogonal $\tau \approx$ 89.7°, leading to eclipsed ^{t}Bu groups (Fig. 2c). Surprisingly, this eclipsed arrangement is preferred over the antiparallel alignment seen in **2** and **3β**, likely because the steric bulk of the ^{t}Bu group prevents such a conformation. The structure is instead stabilized by secondary interactions, such as CH⋯S hydrogen bonding and bowing-induced relief of one radical to reduce phenyl ring electrostatic repulsion. Despite similar hinge and twist angles to **2**, these extreme distortions make **6** unique, leading to the largest S⋯S′ distance (Δ = 6.103(1) Å). The well-defined positions of the ^{t}Bu-groups in **6** contrasts sharply with the rotational disorder observed for smaller alkyl chains in **4–5**, demonstrating how steric bulk restricts molecular flexibility and suppresses dynamic disorder in the crystalline state.

Interdimer interactions and packing motifs. The solid-state packing of radicals **1–6** is governed by a hierarchy of interactions where the primary stabilizations arise from the formation of *cis*-cofacial π-dimers, while the overarching 3D architecture is dictated by secondary interdimer contacts. These are primarily σ-hole-driven chalcogen bonds between electropositive regions on the DTDA sulfur atoms and electronegative sites (lone pairs on exocyclic S, N, or π-systems on adjacent rings). The critical role of these intermolecular interactions is vividly exemplified by the three distinct polymorphs of **3** (Fig. 3), wherein the rich electrostatic landscape leads to distinct ABAB and AA′BB′ packing motifs (Fig. 4) and subtle differences in **SN-II** and **SN-III** type interactions directly dictate the resulting chalcogen-bonded architecture. The nature of the thioalkyl substituent (–SR) in **2–6** plays a critical role in modulating these interactions, leading to two dominant, yet distinct, packing motifs.

Motif I: the ABAB σ-hole optimized packing. The ABAB packing motif, exemplified by **2** and **3α**, consists of slipped π-stack arrangement where each dimer is surrounded by six nearest-neighbor dimer pairs (see Fig. 3). The slippage creates zig-zag chains propagated by highly directional chalcogen bonds (d_3, $d_4 \approx$ 3.29–3.52 Å) between the σ-hole of a DTDA ring on one dimer and a lone pair on the exocyclic sulfur atom of a neighbor. This primary electrostatic architecture is reinforced by edge-to-face interactions between DTDA σ-holes and electronegative π-surface of the phenyl rings. These robust chains are linked into 2D herringbone layers by weaker van der Waals contacts and CH⋯S interactions involving the thioalkyl chains, though these play a secondary role. Connections between these layers are governed by weaker S⋯N (SN-type, Chart 1) electrostatic interactions and dispersion forces, the specific geometry of which (**SN-II** *versus* **SN-III**) is modulated by the thioalkyl group steric and π-stack slippage.

The beta-phase, **3β**, also adopts an ABAB arrangement, but features a distinct packing architecture (Fig. 3 and 4). Unlike **2** and **3α** which utilize exocyclic thioalkyl sulfur atom and DTDA σ-hole interactions, **3β** optimizes DTDA-to-DTDA interactions. At the AB π-stack junctions, dimers adopt an orthogonal head-

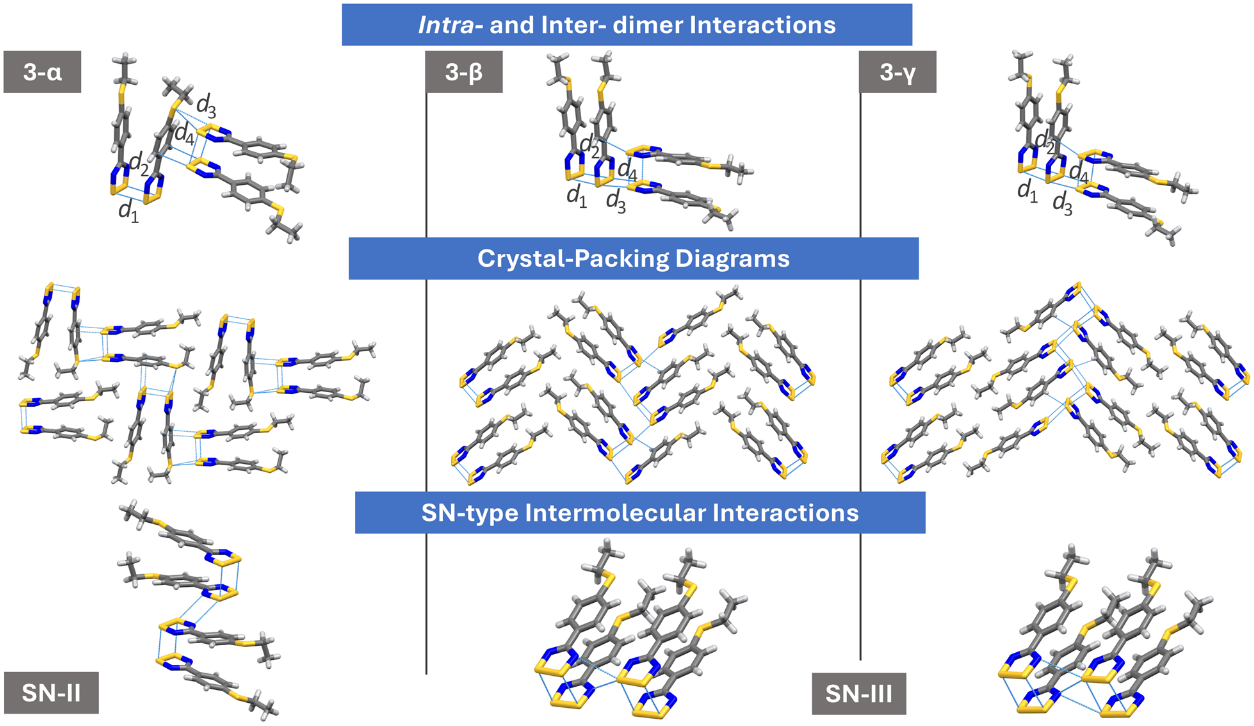

Fig. 3 Summary of intra- and inter-dimer interactions in the three polymorphs of **3** (top), their crystal packing viewed perpendicular to the *ab*-plane (**3α**), or down the *a*-axis (**3β** and **3γ**), and illustrations of the **SN-II** (**3α**) and **SN-III** (**3β** and **3γ**) type intermolecular interactions.

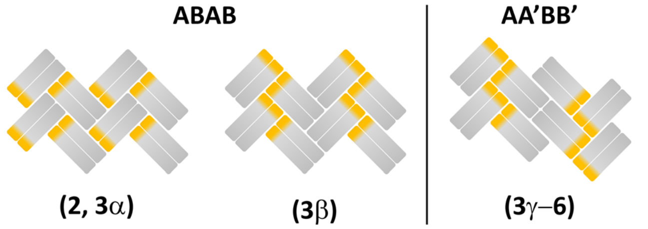

Fig. 4 Schematic comparison of the dominant packing motifs: the two subtypes of ABAB herringbone packing and the AA′BB′ herringbone arrangement that underpins the key structural differences within the series of compounds **2–6**.

to-head orientation that aligns the σ-hole of one DTDA ring with the electronegative regions above a neighboring DTDA or phenyl ring (Fig. 3). This reorientation pushes the ethylthio groups into an orthogonal orientation and buffering regions where they engage in van der Waals contacts rather than strong chalcogen bonding. Consequently, the inter-layer interactions are optimized through staggering of the π-stacks and **SN-III** type contacts. This unique motif maximizes favorable DTDA electrostatic interactions while leveraging alkyl chain dispersion, effectively decoupling the role of the exocyclic sulfur from the primary supramolecular connectivity found in **2** and **3α**.

Motif II: the alkyl-buffered AA′BB′ packing. The AA′BB′ packing motif, observed in **3γ** and **4–6** is characterized by segregated, head-to-head arranged π-stacks. Like **3β**, the strongest intermolecular interactions are short S⋯S′ contacts (d_3, d_4 ≈ 3.41–3.61 Å) at the junctions between the A and B stacks, aligning a DTDA σ-hole with the electronegative regions of a neighboring DTDA or phenyl ring.

In this motif, the alkyl groups are oriented into the spaces between these AA or BB π-stacks, creating a distinct buffering region. Within this region, the dominant stabilizing forces are weak van der Waals interactions and dispersion between the alkyl groups themselves. For linear chains (*e.g.* **3γ** and **4**), the alkyl groups adopt antiperiplanar or *gauche* conformations to minimize steric clashes within a dimer, however, this conformation limits the interdigitation between dimers in the same stack, reducing the cohesive van der Waals energy in these regions. This weakened stabilization within the alkyl buffer layers is a key factor in the divergent thermal behavior (lower melting points and sublimation) observed for **3β** and **4**, which will be discussed in more detail below.

The overall architecture of these AA′BB′ assemblies is further dictated by the alkyl chains bulk. Linear chains facilitate a stratified layered structure of the π-stacks. In contrast, the steric demand of the branched groups **5** (^{i}Pr) and **6** (^{t}Bu) disrupts this layering, forcing the structure into to a more complex zig-zag motif (Fig. 5). This transition highlights how increasing steric bulk modulates the supramolecular hierarchy.

These layered architectures are supported not by strong directional bonds, but a suite of weaker interactions, including CH⋯π, CH⋯S hydrogen bonding and weak SN-type contacts.

Polymorphism. The solid-state behavior of these radicals is marked by a stark contrast in polymorphism. While compounds **1**, **2**, and **4–6**, are monomorphic, as confirmed by

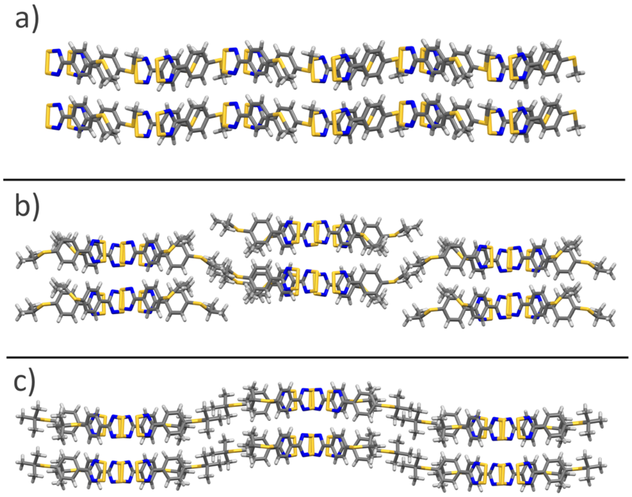

Fig. 5 Tuning layered architecture through steric demand. An illustration comparing (a) the layered ABAB herringbone packing in **2** with the sterically induced modifications of the layered AA′BB′ herringbone packing in **5** (b) and **6** (c), showing a direct correlation between alkyl group bulk (Me ≪ ^{i}Pr < ^{t}Bu) and supramolecular organization.

PXRD (SI), the ethyl derivative **3** exhibits three distinct phases (**3α**, **3β**, and **3γ**) isolated *via* crystallization or vacuum sublimation. This dichotomy mirrors the polymorphism in $\mathbf{M^R}$ (R = Et), though the *cis*-cofacial dimers found in $\mathbf{M^R}$ (R = Me–Bu) predominantly adopt either head-to-tail or head-to-head π-stacks. This suggests there is enough conformational flexibility (the terminal CH_3 group can rotate) to allow the molecule to pack in several nearly equal energetic ways. This creates a delicate energy landscape where slight changes in crystallization conditions (solvent, temperature, cooling rate) or sublimation parameters can lead to different stable phases (**3α**, **3β**, **3γ**).

Analysis of intermolecular contacts and packing

A comparative analysis of the Hirshfeld surfaces and 2D fingerprint plots for the **3(α–γ)** polymorphs provides valuable qualitative insights into the distinct intermolecular interaction patterns, underscoring the structural diversity within this system (see Fig. 6 and S39).[57,66,67] Notably, the prominent sulfur-involved interactions (highlighted in blue) exhibit striking variations across the polymorphs, directly correlating with their differing packing motifs. These chalcogen-driven interactions play a critical role in stabilizing each crystalline form. In **3α**, a unique zig-zag motif of chalcogen–DTDA interactions is observed, characterized by well-defined S⋯S contacts near $d_i = d_e = 1.7$ (Fig. 6), corresponding to the inter-dimer distances d_3 (3.354 Å) and d_4 (3.521 Å).

This contrasts sharply with **3β** and **3γ**, which adopt herringbone packing motifs where the thioalkyl groups primarily act as steric buffers rather than participating in directional chalcogen bonding. This distinction is evident in their more diffuse S⋯S interactions, extending beyond $d_i = d_e = 2.0$ (Fig. 6), a consequence of elongated lateral S⋯S contacts arising from **SN-III** type binding.

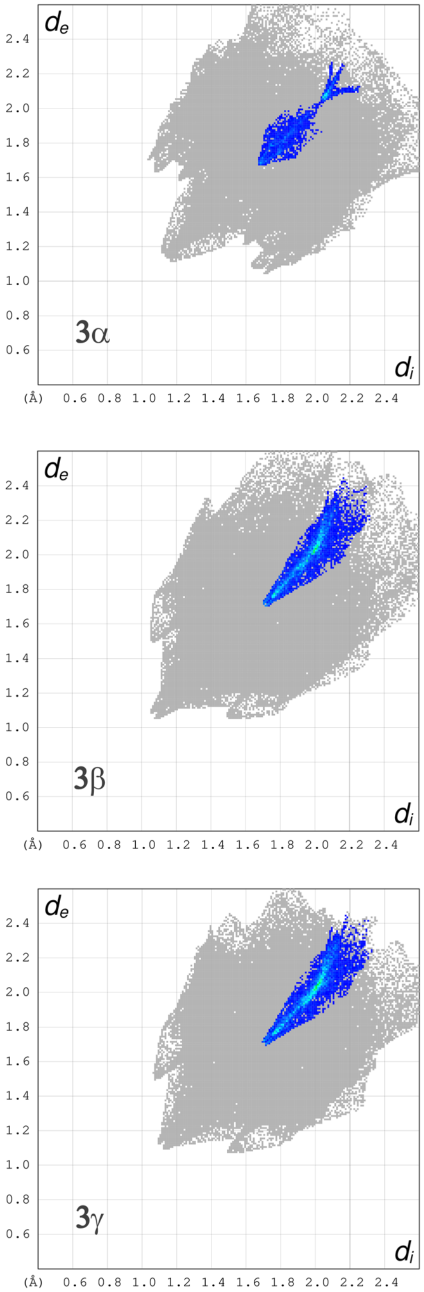

Fig. 6 Hirshfeld 2D fingerprint plots of **3(α–γ)**. Highlighted dots (blue) correspond to sulfur–sulfur contact areas on the Hirshfeld surface.

The divergence in intermolecular connectivity from directed chalcogen interactions in **3α** to sterically modulated packing in **3β**/**3γ** highlights how subtle changes in sulfur-centered electrostatic and dispersion forces can dramatically influence solid-state packing in these DTDAs. Qualitatively, the chalcogen–chalcogen contact surface areas ($d_i = d_e$ = sulfur) account for approximately 2.7% (**3α**), 6.8% (**3β**) and 7.3% (**3γ**) of the total Hirshfeld surface, reflecting geometric differences in lateral S⋯S contacts between polymorphs imposed by **SN-II** and **SN-III** type binding. Beyond sulfur interactions, the 2D fingerprint plots reveal a rich array of additional intermolecular interactions (*e.g.* H⋯H, C⋯H and π-stacking), further underscoring the complexity of the packing landscape in these polymorphs. Analysis of the key geometric parameters (Table 1) reveals clear alkyl-dependent trends across **2–6**. There is a notable inverse correlation (small $\psi \leftrightarrow$ large Δ) between the radical collinearity (ψ) and the intradimer S⋯S′ separation (Δ), where smaller torsion angles often coincide with larger separations, a relationship dictated by the alkyl group conformation. Branched alkyl groups (**5** and **6**) enforce large, near-orthogonal C–C–S–C dihedral angles ($\tau \approx$ 62–90°) and the bulkier ^{t}Bu-group elongates the average interdimer S⋯S′ contact distances (d_3 and d_4) relative to the prototypical system, **1**. The increased steric bulk also favors the AA′BB′ herringbone packing motif.

Despite these significant steric perturbations, the core *cis*-cofacial dimer structure remains remarkably robust. This is evidenced by the consistently minimal hinge ($\phi < 9°$) and torsion ($\psi < 2.3°$ in **3α**, **5**, **6**) angles across the series. The system instead relieves steric and electrostatic strain through molecular-level distortions: elongating Δ, adopting *gauche* conformations, and inducing pronounced molecular bowing, thereby preserving the essential π-dimeric core (see section 7, SI).

Thermal studies

Preliminary thermal gravimetric analysis (TGA) with integrated calorimetry (TG/DSC) was performed on analytically pure compounds, **1–6**. The data (Fig. S19–S24) reveal well-defined melting and sublimation onsets with no significant thermal decomposition (Table S14). Further thermal characterization was conducted using differential scanning calorimetry (DSC) and supplemented in select cases (**3** and **6**) by hot-stage microscopy to visualize the phase transitions.

DSC measurements (2–10 K min^{-1} heating/cooling rates) showed no thermal events prior to melting. The melting and recrystallization temperature ranges are summarized in Table 2. Routine DSC analysis (see Fig. 7 and S25–28) at 2–10 K min^{-1} revealed consistent enthalpies across multiple heating/cooling cycles for **1**, **2**, and **4–6** indicating the thermal robustness without significant decomposition. However, **6** exhibited a small, yet progressive decrease in enthalpies upon repeated cycling, suggesting some sample decomposition may occur (*vide supra*, see Table S15). The thermal behavior of pure **3α** (confirmed by PXRD) was more complex. The initial heating produced a single endotherm, while subsequent cooling cycles displayed multiple exotherms in a narrow range (361–365 K). Further heating/cooling cycles revealed rate-independent behavior, often exhibiting two-stage melting (endotherms at 388–399 K), indicating two independent melting processes.

Table 2 Summary of thermal regions of melting and recrystallization, and thermal hysteresis width determined by DSC[a]

Compound	Melting event (K)	Recrystallization event (K)	Hysteresis range (K)	Post-DSC PXRD phase
1	390–396	356–360	30	**1**
2	430–441	410–416	14	**2**
3α	387–397	369–371	16	**3β**
3β[b]	386–395	364–366	20	**3β**
3γ[b]	386–396	362–366	20	**3β**
4	385–390	353–357	28	**4**
5	370–377	345–350	20	**5**
6	426–434	389–393	33	**6**

[a] For all compounds, all heating and cooling cycles were performed at 10 K min^{-1} unless otherwise stated. [b] Heating and cooling cycles were performed at 2 K min^{-1}.

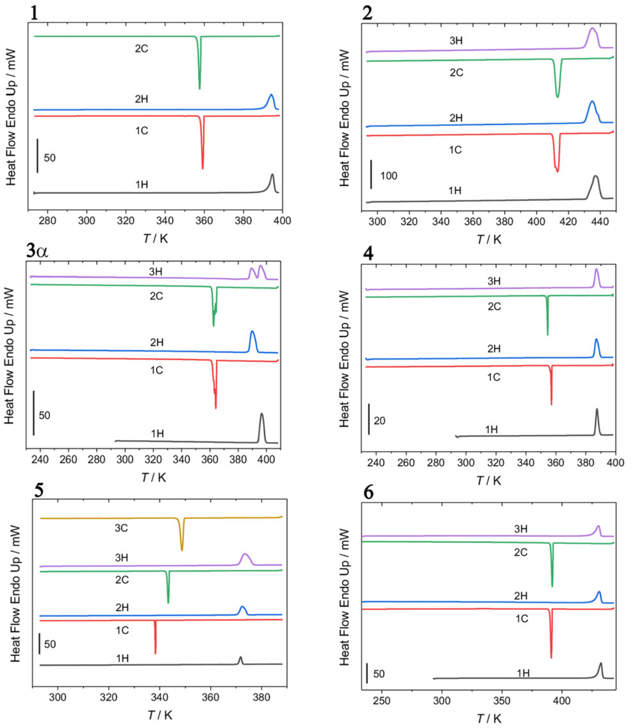

Fig. 7 For compounds **1–3** and **6**, all heating (H) and cooling (C) cycles were performed at 10 K min^{-1} in the DSC measurements. For **4** heating was conducted at 10 K min^{-1} and cooling at 5 K min^{-1}. For **5**, progressive heating/cooling rates were applied: cycle 1H/1C: 2 K min^{-1}; cycle 2H/2C: 5 K min^{-1}; cycle 3H/3C: 10 K min^{-1}.

This suggests concomitant recrystallization[68,69] of two phases of **3** may occur upon cooling, consistent with poorly resolved exotherms (361–365 K). Alternatively, there may be a minor metastable phase undetectable by PXRD but observable *via* DSC that may form. Notably, post-DSC PXRD measurements confirmed the formation of **3β** following melt-recrystallization of **3**. However, careful screening of single crystals obtained from the melt revealed the presence of **3γ**, suggesting this polymorph forms in quantities too low for PXRD detection but possibly observable by DSC. Due to the similarity between PXRD patterns of **3β** and **3γ**, particularly their dominant peak at $2\theta \approx 4.3°$ (assigned to (010) for **3β** and (020) for **3γ**), alongside overlapping weaker reflections, trace detection and differentiation of **3γ** in the presence of **3β** remains challenging.

Therefore, we used hot-stage microscopy to further resolve the phase transition dynamics between the solid and liquid states, beginning with the melting of highly phase-pure **3α** at the onset temperature of ~393 K (SI; see Fig. S29). Upon further heating, plate-like crystals nucleate and grow from the melt at 396 K, which are likely **3β**. Complete melting occurs above 398 K, yielding a paramagnetic liquid. Subsequent cooling to 358 K led to recrystallization and subsequent thermal cycling displayed melting point depression, consistent with DSC results for **3β** (Fig. S27). The predominance of **3β** after DSC thermal cycling indicates its higher thermodynamic stability under these conditions, consistent with the diffraction data (post-DSC PXRD). In contrast, **3α** appears to be a kinetically trapped phase, accessible only through dynamic vacuum sublimation of pure **3** or by recrystallization from the crude reduction mixture (see Fig. S9 and S10).

Together, these results establish **3β** as the thermodynamic product of melt-recrystallization, while **3α** is a kinetic phase accessible only *via* non-equilibrium synthesis (*e.g.* dynamic vacuum sublimation). The detection of **3γ** implies a metastable phase which is thermodynamically supplanted by **3β** under identical conditions. The persistence of **3α** under synthetic conditions reflects a high kinetic barrier for its conversion to **3β**, while **3γ** likely occupies a shallow local minimum on the free-energy surface.

DSC of compound **5** revealed single endotherm and single exotherm events across all tested heating and cooling rates (2, 5, and 10 K min^{-1}), demonstrating fully reversible phase transitions. Notably, **5** exhibited the strongest rate-dependent recrystallization kinetics in the series, with crystallizations shifting by $\Delta T \approx 15$ K over the tested rate range. This distinctive behavior originates from the steric demands and branched geometry of the isopropyl group, which significantly modulates both nucleation barriers and crystal growth dynamics through conformational frustration and alignment constraints necessary for stable lattice formation. In contrast, less hindered methyl and ethyl derivatives (**2** and **3**), linear analogue **4**, and the higher symmetry *tert*-butyl compound **6** all showed minimal rate dependence. Post-DSC PXRD analysis (Fig. S17) confirmed that **5** consistently recrystallizes into its original phase-pure form, demonstrating thermal cycling stability despite its kinetic sensitivity.

The melting temperatures (DSC onset/completion) align well with TGA data (Table S14 and Fig. S19–24). The highest melting points occur for sterically extreme compounds **2** and **6**. The elevated melting point of **2** is attributed to extensive chalcogen bonding and electrostatic interactions within zigzag chains, augmented by crosslinking *via* **SN-III** type interactions (see Chart 1 and Fig. 2). In contrast, the eclipsed arrangement in **6** is energetically favored, while the S⋯π-hole interactions and interlacing ^{t}Bu-groups enhance van der Waals interactions between π-stacks, increasing interfacial contact area and contributing to enhanced thermal stability.

The melting point variation (>50 K across **2**–**6**) far exceeds that reported for $\mathbf{M^R}$ (R = Me–Bu) where the difference between $\mathbf{M^R}$ (R = Me and R = Pr) is <20 K.[16] This stark contrast highlights the pronounced influence of S⋯π and steric interactions on the thermal properties compared to the normal alkyl chain ether derivatives ($\mathbf{M^R}$). All compounds exhibit thermal hysteresis of 18–32 K (Table 2), consistent with other bistable DTDA paramagnetic liquids and significantly broader than the hysteresis observed in the related solid-state bistable systems.[15]

Hot-stage microscopy was performed on **6** as a representative sample to visualize the thermal events measured by DSC. The neat crystalline sample (295 K) started melting at 428 K and was essentially completed at 429 K, as shown in Fig. 8. Recrystallization in the supercooled liquid phase occurs rapidly at 385 K. These observations are in good agreement with the melting and crystallization temperatures determined through DSC given in Table 2, indicating that the events described in DSC correspond to slow melting and fast recrystallization.

Magnetic studies

The variable temperature magnetic characterization was performed on a vibrating sample magnetometer (VSM) under an applied dc field of 1 T (SI). All radicals **1**–**6** exhibit essentially diamagnetic behavior ($\chi T \approx 0$) in their crystalline state at 300 K (see Fig. 9 and S31). Upon melting (confirmed by DSC) each compound shows an abrupt increase in χT to 0.25–0.30 cm^3 K mol^{-1} indicating the formation of paramagnetic liquids. The values are slightly reduced from the ideal Curie behavior (χT = 0.375 cm^3 K mol^{-1} for $S = \frac{1}{2}$ and a value of $g = 2.00$) suggesting weak antiferromagnetic exchange in the liquid phase, consistent with prior reports.[10]

Thermal hysteresis is clearly observed during cooling cycles, with χT remaining elevated until recrystallization (as confirmed by DSC and hot-stage microscopy) at which point it drops sharply to near-zero values (Fig. 9). Compounds **1**–**5** display reproducible thermal hysteresis ($\Delta \approx 15$–30 K) that was independent of the heating/cooling rate and in excellent agreement with the DSC results. This behavior matches established literature precedents for related DTDA paramagnetic liquids observed by either EPR or magnetometry (Scheme 1).[10,11,43,44] For **6**, χT exhibits thermal hysteresis during the first heating/cooling cycle, consistent with DSC-determined melting and recrystallization. However, this behavior is not reproducible in subsequent cycles, possibly due to persistent sample displacement/centering issues despite testing various preparation methods and sample holder configurations. Notably, DSC measurements confirm **6** does exhibit reversible melt-recrystallization behavior comparable to **1**–**5**, suggesting the magnetic measurement challenges are likely experimental rather than intrinsic to the material.

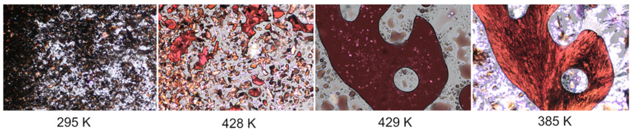

Fig. 8 Hot-stage microscopy of **6** showing one heating and cooling cycle (~10 K min^{-1}) starting from neat, microcrystalline material (far left) obtained from vacuum sublimation. The onset of melting occurs at 428 K and is nearly complete at 429 K and recrystallizes from the supercooled liquid at 385 K (far right).

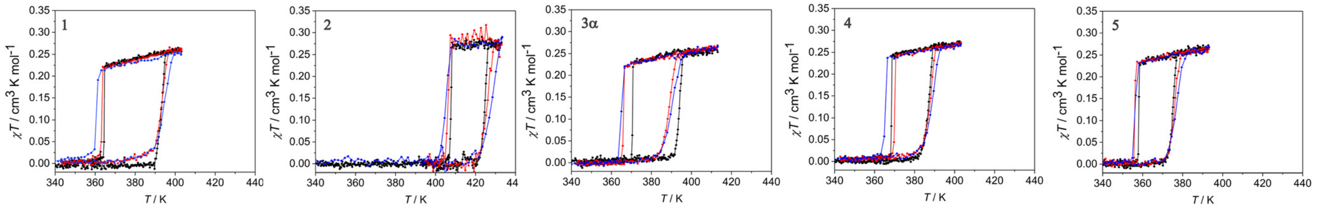

Fig. 9 The temperature dependence of χT measured for **1–5**. For all compounds, heating and cooling cycles were performed at 2 (black line), 5 (red line) and 10 (blue line) K min^{-1}. See Fig. S31 for compound **6**.

The magnetic data are in excellent agreement with the DSC results, linking the observed magnetic bistability to the thermal hysteresis associated with melting and recrystallization from the supercooled liquid phase. As shown in Fig. 9, radicals **1–5** exhibit reproducible temperature-dependent magnetic properties, consistent with those reported for DTDA paramagnetic liquids.

While the complex thermal behavior of **3** in DSC is not immediately evident in the magnetic data, detailed analysis reveals that all three polymorphs have nearly identical melting onsets (±3 K), complicating phase composition determination by DSC alone. Notably, DSC measurements starting from phase-pure **3α** or **3γ** consistently yield **3β**, as confirmed by post-DSC PXRD.

Although VSM temperature control is less precise than DSC, the sharp increase in χT near 391 K for neat **3α** aligns with melting to a paramagnetic liquid, while the recrystallization at 370 K matches DSC observations. In subsequent heating cycles, the onset of the χT increase becomes more gradual (~382–384 K), likely due to melting of a phase mixture dominated by **3β**, as suggested by prior results. Crucially, the thermal hysteresis ($\Delta \approx 15$ K) remains consistent across measurements, independent of phase composition.

Discussion

The paramagnetic liquid phases in radicals **1–6** all occur at relatively high temperatures, above 370 K, in contrast to the known DTDA paramagnetic liquids that melt below 330 K.[10,11,43,44] The paramagnetic liquid phase of the prototypical **1** has likely eluded researchers for this reason, as its high-temperature magnetic properties have not been studied before to our knowledge, although thermal analysis by DSC has been reported.[70]

The relatively high melting points in **1–6** could arise from the high dimensionality of strong intermolecular interactions in their crystal structures, enabled by the zig-zag- and herringbone packing motifs in **2–6** which permeate throughout entire crystallographic axes. The packing of 2-tolyl-substituted DTDA also consists of similar chain motifs *via* **SN-IV** type interactions, but its melting point is around 320 K as evidenced by an increase in EPR intensity corresponding to melting to a paramagnetic liquid.[44]

The polymorphism observed in the ethyl derivative **3** parallels that of $\mathbf{M^R}$ (R = Et),[16] where both compounds represent critical turning points in their respective radical series. In each case, the dominant packing motif changes because of varying degrees of steric effects imposed by the alkyl substituent leading to distinct polymorphic behavior.

For $\mathbf{M^R}$ (R = Et), the β- and γ-phases are linked by a single-crystal-to-single-crystal (SCSC) transition, wherein the equilibrium between monomeric and dimeric units shifts reversibly, resulting in hysteretic magnetic bistability. In contrast, **3α** and **3β** do not interconvert *via* an SCSC transition under DSC conditions, despite both being isolable under specific experimental protocols. Instead, **3β** emerges as the thermodynamically stable phase, dominating the phase landscape upon thermal cycling. This divergence in polymorphic behavior highlights the nuanced role of alkyl substitution in modulating solid-state packing and phase stability. While $\mathbf{M^R}$ (R = Et) exhibits dynamic structural flexibility (enabling SCSC transitions), the ethyl derivative **3** appears to adopt more rigid packing arrangements, with **3α** and **3γ** trapped as metastable states. The persistence of **3β** across DSC cycles suggests that kinetic control during crystallization rather than reversible structural rearrangement governs the polymorphism of **3**.

Conclusions

The synthesis and structural characterization of a series of *p*-alkylthio substituted phenyl-DTDAs **2** (R = SMe), **3** (R = SEt), **4** (R = S^{n}Pr), **5** (R = S^{i}Pr), **6** (R = S^{t}Bu) revealed two distinctive packing motifs: zig-zag chains of *cis*-cofacial dimers mediated by chalcogen–chalcogen bonding in **2** and **3α**, and herringbones *via* chalcogen-π bonding in **3β–6**. Thermal and magnetic studies revealed that **1–6**, with **1** being the previously reported phenyl-DTDA, undergo melting to paramagnetic liquid phases, which crystallize upon supercooling resulting in magnetic bistability. The newly discovered paramagnetic liquid phase and supercooling-driven magnetic bistability of **1** suggests that the phenomenon could be more prevalent than what is currently known among DTDAs and other types of radicals. Given that the radicals known to have paramagnetic liquid phases tend to have relatively low melting points, high-temperature calorimetry and magnetic susceptibility measurements of known radicals could reveal novel phase transitions in the development of functional radical materials.

The thioether substitution of DTDAs also provides ample opportunities for future work as post-synthetic modification might allow the realization of DTDA-based sulfonium salts or chiral sulfoxides. Small synthetic modifications such as these might enable incorporating new properties like chirality into paramagnetic liquids, liquid crystalline materials, and other desirable properties towards multifunctional soft materials.

Experimental

The full synthetic details, thermal analytical (DSC, TGA, HSM, EA), crystallography (SCXRD/PXRD), and magnetic details (VSM) are available in SI.

Author contributions

JT, AN, OGP, APP and AM contributed to the methodology development and spectroscopic characterization of all compounds. JT, AN, ML, and AM performed the X-ray diffraction studies, as well as thermal and analytical characterization. IO performed the VSM measurements. AM conceptualized and supervised the research. JT and AM led the manuscript writing and revisions with critical input from all authors. All authors reviewed and approved the final version of the manuscript.

Conflicts of interest

There are no conflicts to declare.

Data availability

The original contributions of this study are included in the article and supplementary information (SI). Raw IR, PXRD, VSM, TGA, DSC, and hot-stage microscopy (HSM) data are available on Figshare at [**https://doi.org/10.6084/m9.figshare.29954279**] or can be obtained from the authors upon request.

Supplementary information is available. See DOI: **https://doi.org/10.1039/d5qi01391g**.

CCDC 2457524–2457531 contain the supplementary crystallographic data for this paper.[71a–h]

Acknowledgements

This work was supported by the Academy of Finland (projects 358156, 336456, 333565) and the University of Jyväskylä, and the authors are grateful for technical and human support provided by SGIker (UPV/EHU/ERDF, EU), especially the fruitful discussions with Dr I. Orue.

References

1 I. Ratera and J. Veciana, Playing with organic radicals as building blocks for functional molecular materials, *Chem. Soc. Rev.*, 2012, **41**, 303–349.

2 J. M. Rawson, A. Alberola and A. Whalley, Thiazyl radicals: old materials for new molecular devices, *J. Mater. Chem.*, 2006, **16**, 2560–2575.

3 D. A. Haynes, Crystal engineering with dithiadiazolyl radicals, *CrystEngComm*, 2011, **13**, 4793–4805.

4 Y. Beldjoudi, M. A. Nascimento, Y. J. Cho, H. Yu, H. Aziz, D. Tonouchi, K. Eguchi, M. M. Matsushita, K. Awaga, I. Osorio-Roman, C. P. Constantinides and J. M. Rawson, Multifunctional Dithiadiazolyl Radicals: Fluorescence, Electroluminescence, and Photoconducting Behavior in Pyren-1′-yl-dithiadiazolyl, *J. Am. Chem. Soc.*, 2018, **140**, 6260–6270.

5 Y. Beldjoudi, A. Arauzo, J. Campo, E. L. Gavey, M. Pilkington, M. A. Nascimento and J. M. Rawson, Structural, Magnetic, and Optical Studies of the Polymorphic 9′-Anthracenyl Dithiadiazolyl Radical, *J. Am. Chem. Soc.*, 2019, **141**, 6875–6889.

6 Y. Beldjoudi, A. Arauzo, F. Palacio, M. Pilkington and J. M. Rawson, Studies on a "Disappearing Polymorph": Thermal and Magnetic Characterization of α-*p*-$NCC_6F_4CNSSN^•$, *J. Am. Chem. Soc.*, 2016, **138**, 16779–16786.

7 D. Leckie, M. Harb, N. Mroz, J. D. Wrixon, J. Campo, A. Arauzo, H. Bakhshi, M. Pilkington and J. M. Rawson, A Spontaneous Magnetic Moment in an Organic Radical: Synthesis and Characterization of Benzodioxepinyl-1,3,2-dithiazolyl, *J. Am. Chem. Soc.*, 2024, **146**, 31371–31376.

8 G. C. Borg, H. K. S. Young, M. B. Mills, J. W. Mastrandrea, F. Benner, S. Demir, A. J. Lough, P. D. Boyle and K. E. Preuss, Polymorphism of a planar neutral radical: magnetic and optical implications, *Can. J. Chem.*, 2024, **102**, 745–752.

9 W. V. F. Brooks, N. Burford, J. Passmore, M. J. Schriver and L. H. Sutcliffe, Paramagnetic liquids: the preparation and characterisation of the thermally stable radical $Bu^tCNSNS^•$ and its quantitative photochemically symmetry allowed rearrangement to a second stable radical Bu^tCNSSN, *J. Chem. Soc., Chem. Commun.*, 1987, 69–71.

10 H. Du, R. C. Haddon, I. Krossing, J. Passmore, J. M. Rawson and M. J. Schriver, Thermal hysteresis in dithiadiazolyl and dithiazolyl radicals induced by supercooling of paramagnetic liquids close to room temperature: a study of $F_3CCNSSN$ and an interpretation of the behaviour of $F_3CCSNSCCF_3$, *Chem. Commun.*, 2002, 1836–1837.

11 K. V. Shuvaev, A. Decken, F. Grein, T. S. M. Abedin, L. K. Thompson and J. Passmore, $NC–(CF_2)_4–CNSSN^•$ containing 1,2,3,5-dithiadiazolyl radical dimer exhibiting triplet excited states at low temperature and thermal hysteresis on melting–solidification: structural, spectroscopic, and magnetic characterization, *Dalton Trans.*, 2008, 4029–4037.

12 W. Fujita, K. Awaga, Y. Nakazawa, K. Saito and M. Sorai, Complex phase transitions in stable thiazyl radicals: spin-gap, antiferromagnetic ordering and double melting, *Chem. Phys. Lett.*, 2002, **352**, 348–352.

13 S. Brownridge, H. Du, S. A. Fairhurst, R. C. Haddon, H. Oberhammer, S. Parsons, J. Passmore, M. J. Schriver,

L. H. Sutcliffe and N. P. C. Westwood, The isolation, characterisation, gas phase electron diffraction and crystal structure of the thermally stable radical $[CF_3CSNSCCF_3]^{\bullet}$, *J. Chem. Soc., Dalton Trans.*, 2000, 3365–3382.

14 W. Fujita and K. Awaga, Room-Temperature Magnetic Bistability in Organic Radical Crystals, *Science*, 1999, **286**, 261–262.

15 M. B. Mills, T. Wohlhauser, B. Stein, W. R. Verduyn, E. Song, P. Dechambenoit, M. Rouzières, R. Clérac and K. E. Preuss, Magnetic Bistability in Crystalline Organic Radicals: The Interplay of H-bonding, Pancake Bonding, and Electrostatics in 4-(2′-Benzimidazolyl)-1,2,3,5-dithiadiazolyl, *J. Am. Chem. Soc.*, 2018, **140**, 16904–16908.

16 Y. Beldjoudi, R. Sun, A. Arauzo, J. Campo, R. J. Less and J. M. Rawson, Structural Variations in the Dithiadiazolyl Radicals *p*-ROC_6F_4CNSSN (R = Me, Et, ^{n}Pr, ^{n}Bu): A Case Study of Reversible and Irreversible Phase Transitions in *p*-$EtOC_6F_4CNSSN$, *Cryst. Growth Des.*, 2018, **18**, 179–188.

17 A. J. Banister, N. Bricklebank, I. Lavender, J. M. Rawson, C. I. Gregory, B. K. Tanner, W. Clegg, M. R. J. Elsegood and F. Palacio, Spontaneous Magnetization in a Sulfur–Nitrogen Radical at 36 K, *Angew. Chem., Int. Ed. Engl.*, 1996, **35**, 2533–2535.

18 J. Luzón, J. Campo, F. Palacio, G. J. McIntyre, A. E. Goeta, E. Ressouche, C. M. Pask and J. M. Rawson, Spin-density distribution in the new molecular magnet *p*,-$O_2N{\cdot}C_6F_4{\cdot}CNSSN$, *Phys. B: Condens. Matter*, 2003, **335**, 1–5.

19 A. Mailman, C. M. Robertson, S. M. Winter, P. A. Dube and R. T. Oakley, The Importance of Electronic Dimensionality in Multiorbital Radical Conductors, *Inorg. Chem.*, 2019, **58**, 6495–6506.

20 A. Mailman, J. W. L. Wong, S. M. Winter, R. C. M. Claridge, C. M. Robertson, A. Assoud, W. Yong, E. Steven, P. A. Dube, J. S. Tse, S. Desgreniers, R. A. Secco and R. T. Oakley, Fine Tuning the Performance of Multiorbital Radical Conductors by Substituent Effects, *J. Am. Chem. Soc.*, 2017, **139**, 1625–1635.

21 T. S. Cameron, M. T. Lemaire, J. Passmore, J. M. Rawson, K. V. Shuvaev and L. K. Thompson, Preparation and Solid-State Characterization of the Novel Mixed Biradical $^{\bullet}$NSNSC–CNSSN$^{\bullet}$, *Inorg. Chem.*, 2005, **44**, 2576–2578.

22 A. Decken, T. S. Cameron, J. Passmore, J. M. Rautiainen, R. W. Reed, K. V. Shuvaev and L. K. Thompson, Characterization of the Diradical $^{\bullet}$NSNSC–CNSSN$^{\bullet}$ and $[NSNSC{-}CNSSN][MF_6]_n$ (n = 1, 2). The First Observation of an Excited Triplet State in Dimers of 7π –CNSSN$^{\bullet}$ Radicals, *Inorg. Chem.*, 2007, **46**, 7436–7457.

23 X. Yu, A. Mailman, K. Lekin, A. Assoud, C. M. Robertson, B. C. Noll, C. F. Campana, J. A. K. Howard, P. A. Dube and R. T. Oakley, Semiquinone-Bridged Bisdithiazolyl Radicals as Neutral Radical Conductors, *J. Am. Chem. Soc.*, 2012, **134**, 2264–2275.

24 A. Mailman, S. M. Winter, X. Yu, C. M. Robertson, W. Yong, J. S. Tse, R. A. Secco, Z. Liu, P. A. Dube, J. A. K. Howard and R. T. Oakley, Crossing the Insulator-to-Metal Barrier with a Thiazyl Radical Conductor, *J. Am. Chem. Soc.*, 2012, **134**, 9886–9889.

25 A. Iwasaki, L. Hu, R. Suizu, K. Nomura, H. Yoshikawa, K. Awaga, Y. Noda, K. Kanai, Y. Ouchi, K. Seki and H. Ito, Interactive Radical Dimers in Photoconductive Organic Thin Films, *Angew. Chem., Int. Ed.*, 2009, **48**, 4022–4024.

26 A. W. Cordes, R. C. Haddon, R. T. Oakley, L. F. Schneemeyer, J. V. Waszczak, K. M. Young and N. M. Zimmerman, Molecular semiconductors from bifunctional dithia- and diselenadiazolyl radicals. Preparation and solid-state structural and electronic properties of 1,4-$[(E_2N_2C)C_6H_4(CN_2E_2)]$ (E = sulfur, selenium), *J. Am. Chem. Soc.*, 1991, **113**, 582–588.

27 P. Commins, A. Bernard Dippenaar, L. Li, H. Hara, D. A. Haynes and P. Naumov, Mechanically compliant single crystals of a stable organic radical, *Chem. Sci.*, 2021, **12**, 6188–6193.

28 G. R. Desiraju, Crystal Engineering: A Holistic View, *Angew. Chem., Int. Ed.*, 2007, **46**, 8342–8356.

29 D. Bates, C. M. Robertson, A. A. Leitch, P. A. Dube and R. T. Oakley, Magnetic Bistability in Naphtho-1,3,2-dithiazolyl: Solid State Interconversion of a Thiazyl π-Radical and Its N–N σ-Bonded Dimer, *J. Am. Chem. Soc.*, 2018, **140**, 3846–3849.

30 J. L. Brusso, O. P. Clements, R. C. Haddon, M. E. Itkis, A. A. Leitch, R. T. Oakley, R. W. Reed and J. F. Richardson, Bistabilities in 1,3,2-Dithiazolyl Radicals, *J. Am. Chem. Soc.*, 2004, **126**, 8256–8265.

31 T. Tanaka, W. Fujita and K. Awaga, Pressure effects on magnetic bistability in a heterocyclic thiazyl radical TTTA, *Chem. Phys. Lett.*, 2004, **393**, 150–152.

32 S. Vela, F. Mota, M. Deumal, R. Suizu, Y. Shuku, A. Mizuno, K. Awaga, M. Shiga, J. J. Novoa and J. Ribas-Arino, The key role of vibrational entropy in the phase transitions of dithiazolyl-based bistable magnetic materials, *Nat. Commun.*, 2014, **5**, 1–9.

33 K. Lekin, H. Phan, S. M. Winter, J. W. L. Wong, A. A. Leitch, D. Laniel, W. Yong, R. A. Secco, J. S. Tse, S. Desgreniers, P. A. Dube, M. Shatruk and R. T. Oakley, Heat, Pressure and Light-Induced Interconversion of Bisdithiazolyl Radicals and Dimers, *J. Am. Chem. Soc.*, 2014, **136**, 8050–8062.

34 K. Lekin, S. M. Winter, L. E. Downie, X. Bao, J. S. Tse, S. Desgreniers, R. A. Secco, P. A. Dube and R. T. Oakley, Hysteretic Spin Crossover between a Bisdithiazolyl Radical and Its Hypervalent σ-Dimer, *J. Am. Chem. Soc.*, 2010, **132**, 16212–16224.

35 A. K. Hoffmann and A. T. Henderson, A New Stable Free Radical: Di-*t*-Butylnitroxide, *J. Am. Chem. Soc.*, 1961, **83**, 4671–4672.

36 W. D. Blackley and R. R. Reinhard, A New Stable Radical, Bis(trifluoromethyl)Nitroxide, *J. Am. Chem. Soc.*, 1965, **87**, 802–805.

37 R. Tamura, Y. Uchida and N. Ikuma, Paramagnetic all-organic chiral liquid crystals, *J. Mater. Chem.*, 2008, **18**, 2872–2876.

38 A. Dragulescu-Andrasi, A. S. Filatov, R. T. Oakley, X. Li, K. Lekin, A. Huq, C. Pak, S. M. Greer, J. McKay, M. Jo, J. Lengyel, I. Hung, E. Maradzike, A. E. I. DePrince, S. A. Stoian, S. Hill, Y.-Y. Hu and M. Shatruk, Radical Dimerization in a Plastic Organic Crystal Leads to Structural and Magnetic Bistability with Wide Thermal Hysteresis, *J. Am. Chem. Soc.*, 2019, **141**, 17989–17994.

39 Y. Uchida, N. Ikuma, R. Tamura, S. Shimono, Y. Noda, J. Yamauchi, Y. Aoki and H. Nohira, Unusual intermolecular magnetic interaction observed in an all-organic radical liquid crystal, *J. Mater. Chem.*, 2008, **18**, 2950–2952.

40 K. Suzuki, Y. Uchida, R. Tamura, S. Shimono and J. Yamauchi, Observation of positive and negative magneto-LC effects in all-organic nitroxide radical liquid crystals by EPR spectroscopy, *J. Mater. Chem.*, 2012, **22**, 6799–6806.

41 K.-A. Hansen and J. P. Blinco, Nitroxide radical polymers – a versatile material class for high-tech applications, *Polym. Chem.*, 2018, **9**, 1479–1516.

42 A. Bousseksou, G. Molnár, L. Salmon and W. Nicolazzi, Molecular spin crossover phenomenon: recent achievements and prospects, *Chem. Soc. Rev.*, 2011, **40**, 3313–3335.

43 D. A. Haynes, E. J. L. McInnes, J. Passmore and J. M. Rawson, Epr Studies of the Bistability in CF_3CNSSN, *Phosphorus, Sulfur Silicon Relat. Elem.*, 2004, **179**, 869–873.

44 Y. Beldjoudi, D. A. Haynes, J. J. Hayward, W. J. Manning, D. R. Pratt and J. M. Rawson, Preparation and crystal structures of the isomeric series 4-tolyl-1,2,3,5-dithiadiazolyl, $(o\text{-}MeC_6H_4CNSSN)_2$, $(m\text{-}MeC_6H_4CNSSN)_2$ and $(p\text{-}MeC_6H_4CNSSN)_2$, *CrystEngComm*, 2013, **15**, 1107–1113.

45 M. E. Itkis, X. Chi, A. W. Cordes and R. C. Haddon, Magneto-Opto-Electronic Bistability in a Phenalenyl-Based Neutral Radical, *Science*, 2002, **296**, 1443–1445.

46 M. Strydom and D. A. Haynes, A Cambridge Structural Database Study of Pancake Bonding and Geometry in Dithiadiazolyls, *Cryst. Growth Des.*, 2024, **24**, 6311–6325.

47 A. D. Bond, D. A. Haynes, C. M. Pask and J. M. Rawson, Concomitant polymorphs: structural studies on the trimorphic dithiadiazolyl radical, ClCNSSN, *J. Chem. Soc., Dalton Trans.*, 2002, 2522–2531.

48 C. S. Clarke, S. I. Pascu and J. M. Rawson, Further studies on the polymorphic dithiadiazolyl radical, ClCNSSN, *CrystEngComm*, 2004, **6**, 79–82.

49 C. Knapp, E. Lork, K. Gupta and R. Mews, Structure Investigations on 4-Halo-1,2,3,5-dithiadiazolyl Radicals $XCNSSN^•$ (X = F, Cl, Br): The Shortest Intradimer S⋯S Distance in Dithiadiazolyl Dimers, *Z. Anorg. Allg. Chem.*, 2005, **631**, 1640–1644.

50 D. A. Haynes and J. M. Rawson, Molecular Electrostatic Potential as a Predictor of Supramolecular Synthons in Non-Hydrogen-Bonded Systems: Application to Heavier p-Block Systems, *Eur. J. Inorg. Chem.*, 2018, **2018**, 3554–3564.

51 M. A. Nascimento, E. Heyer, R. J. Less, C. M. Pask, A. Arauzo, J. Campo and J. M. Rawson, An Investigation of Halogen Bonding as a Structure-Directing Interaction in Dithiadiazolyl Radicals, *Cryst. Growth Des.*, 2020, **20**, 4313–4324.

52 M. B. Mills, H. K. S. Young, G. Wehrle, W. R. Verduyn, X. Feng, P. D. Boyle, P. Dechambenoit, E. R. Johnson and K. E. Preuss, Noncovalent Interactions in Organic Radicals: Pancake, σ-Hole, and H-Bonding in $F_2HbimDTDA$, *Cryst. Growth Des.*, 2021, **21**, 5669–5677.

53 P. Politzer, J. S. Murray and T. Clark, Halogen bonding and other σ-hole interactions: a perspective, *Phys. Chem. Chem. Phys.*, 2013, **15**, 11178–11189.

54 A. Frontera and A. Bauzá, On the Importance of σ–Hole Interactions in Crystal Structures, *Crystals*, 2021, **11**, 1205.

55 J. S. Murray, P. Lane, T. Clark and P. Politzer, σ-hole bonding: molecules containing group VI atoms, *J. Mol. Model*, 2007, **13**, 1033–1038.

56 C. S. Clarke, D. A. Haynes, J. N. B. Smith, A. S. Batsanov, J. A. K. Howard, S. I. Pascu and J. M. Rawson, The effect of fluorinated aryl substituents on the crystal structures of 1,2,3,5-dithiadiazolyl radicals, *CrystEngComm*, 2010, **12**, 172–185.

57 J. M. Cole, C. M. Aherne, P. G. Waddell, A. J. Banister, A. S. Batsanov and J. A. K. Howard, Solid-state effects of monofluorophenyl substitution in dithiadiazolyl radicals: Impact on S⋯S and S⋯N interactions and their classification *via* Hirshfeld surfaces and fingerprint plots, *Polyhedron*, 2012, **45**, 61–70.

58 K. T. Mahmudov, M. N. Kopylovich, M. F. C. G. da Silva and A. J. L. Pombeiro, Chalcogen bonding in synthesis, catalysis and design of materials, *Dalton Trans.*, 2017, **46**, 10121–10138.

59 R. T. Boeré, R. T. Oakley and R. W. Reed, Preparation of N, N,N′-tris(trimethylsilyl)amidines; a convenient route to unsubstituted amidines, *J. Organomet. Chem.*, 1987, **331**, 161–167.

60 A. Vegas, A. Pérez-Salazar, A. J. Banister and R. G. Hey, Crystal structure of 4-phenyl-1,2-dithia-3,5-diazole dimer, *J. Chem. Soc., Dalton Trans.*, 1980, 1812–1815.

61 A. Bondi, van der Waals Volumes and Radii, *J. Phys. Chem.*, 1964, **68**, 441–451.

62 M. Mantina, A. C. Chamberlin, R. Valero, C. J. Cramer and D. G. Truhlar, Consistent van der Waals Radii for the Whole Main Group, *J. Phys. Chem. A*, 2009, **113**, 5806–5812.

63 S. Alvarez, A cartography of the van der Waals territories, *Dalton Trans.*, 2013, **42**, 8617–8636.

64 S. Domagała, K. Kosc, S. W. Robinson, D. A. Haynes and K. Woźniak, Dithiadiazolyl Radicals—Structures and Charge Densities of Their Crystals and Co-Crystal, *Cryst. Growth Des.*, 2014, **14**, 4834–4848.

65 T. Iijima, S. Tsuchiya and M. Kimura, The Molecular Structure of Dimethyl Sulfide, *Bull. Chem. Soc. Jpn.*, 1977, **50**, 2564–2567.

66 M. A. Spackman and D. Jayatilaka, Hirshfeld surface analysis, *CrystEngComm*, 2009, **11**, 19–32.

67 P. R. Spackman, M. J. Turner, J. J. McKinnon, S. K. Wolff, D. J. Grimwood, D. Jayatilaka and M. A. Spackman, CrystalExplorer: a program for Hirshfeld surface analysis,

visualization and quantitative analysis of molecular crystals, *J. Appl. Crystallogr.*, 2021, **54**, 1006–1011.

68 J. Bernstein, R. J. Davey and J.-O. Henck, Concomitant Polymorphs, *Angew. Chem., Int. Ed.*, 1999, **38**, 3440–3461.

69 Y. Su, J. Xu, Q. Shi, L. Yu and T. Cai, Polymorphism of griseofulvin: concomitant crystallization from the melt and a single crystal structure of a metastable polymorph with anomalously large thermal expansion, *Chem. Commun.*, 2018, **54**, 358–361.

70 S. W. Robinson, D. A. Haynes and J. M. Rawson, Co-crystal formation with 1,2,3,5-dithiadiazolyl radicals, *CrystEngComm*, 2013, **15**, 10205–10211.

71 (*a*) CCDC 2457524: Experimental Crystal Structure Determination, 2025, DOI: **10.5517/ccdc.csd.cc2nh7zd**; (*b*) CCDC 2457525: Experimental Crystal Structure Determination, 2025, DOI: **10.5517/ccdc.csd.cc2nh80g**; (*c*) CCDC 2457526: Experimental Crystal Structure Determination, 2025, DOI: **10.5517/ccdc.csd.cc2nh81h**; (*d*) CCDC 2457527: Experimental Crystal Structure Determination, 2025, DOI: **10.5517/ccdc.csd.cc2nh82j**; (*e*) CCDC 2457528: Experimental Crystal Structure Determination, 2025, DOI: **10.5517/ccdc.csd.cc2nh83k**; (*f*) CCDC 2457529: Experimental Crystal Structure Determination, 2025, DOI: **10.5517/ccdc.csd.cc2nh84l**; (*g*) CCDC 2457530: Experimental Crystal Structure Determination, 2025, DOI: **10.5517/ccdc.csd.cc2nh85m**; (*h*) CCDC 2457531: Experimental Crystal Structure Determination, 2025, DOI: **10.5517/ccdc.csd.cc2nh86n**.